Biomedical Optics EXPRESS

Semi-automated discrimination of retinal pigmented epithelial cells in two-photon fluorescence images of mouse retinas

Nathan S. Alexander,[1,3] Grazyna Palczewska,[2] and Krzysztof Palczewski[1,*]

[1]*Department of Pharmacology, Cleveland Center for Membrane and Structural Biology, School of Medicine, Case Western Reserve University, Cleveland, OH 44106, USA*
[2]*Polgenix Inc., 11000 Cedar Ave, Cleveland, Ohio 44106, USA*
[3]*nsa36@case.edu*
[*]*kxp65@case.edu*

Abstract: Automated image segmentation is a critical step toward achieving a quantitative evaluation of disease states with imaging techniques. Two-photon fluorescence microscopy (TPM) has been employed to visualize the retinal pigmented epithelium (RPE) and provide images indicating the health of the retina. However, segmentation of RPE cells within TPM images is difficult due to small differences in fluorescence intensity between cell borders and cell bodies. Here we present a semi-automated method for segmenting RPE cells that relies upon multiple weak features that differentiate cell borders from the remaining image. These features were scored by a search optimization procedure that built up the cell border in segments around a nucleus of interest. With six images used as a test, our method correctly identified cell borders for 69% of nuclei on average. Performance was strongly dependent upon increasing retinosome content in the RPE. TPM image analysis has the potential of providing improved early quantitative assessments of diseases affecting the RPE.

©2015 Optical Society of America

OCIS codes: (170.3880) Medical and biological imaging; (170.2520) Fluorescence microscopy; (100.2960) Image analysis.

References and links

1. N. M. Bressler, "Age-related macular degeneration is the leading cause of blindness," JAMA **291**(15), 1900–1901 (2004).
2. R. Kolár, R. Laemmer, J. Jan, and ChY. Mardin, "The segmentation of zones with increased autofluorescence in the junctional zone of parapapillary atrophy," Physiol. Meas. **30**(5), 505–516 (2009).
3. A. Roorda, Y. Zhang, and J. L. Duncan, "High-resolution in vivo imaging of the RPE mosaic in eyes with retinal disease," Invest. Ophthalmol. Vis. Sci. **48**(5), 2297–2303 (2007).
4. G. Palczewska, Z. Dong, M. Golczak, J. J. Hunter, D. R. Williams, N. S. Alexander, and K. Palczewski, "Noninvasive two-photon microscopy imaging of mouse retina and retinal pigment epithelium through the pupil of the eye," Nat. Med. **20**(7), 785–789 (2014).
5. Y. Imanishi, M. L. Batten, D. W. Piston, W. Baehr, and K. Palczewski, "Noninvasive two-photon imaging reveals retinyl ester storage structures in the eye," J. Cell Biol. **164**(3), 373–383 (2004).
6. A. A. Dima, J. T. Elliott, J. J. Filliben, M. Halter, A. Peskin, J. Bernal, M. Kociolek, M. C. Brady, H. C. Tang, and A. L. Plant, "Comparison of segmentation algorithms for fluorescence microscopy images of cells," Cytometry A **79**(7), 545–559 (2011).
7. J.-D. Ding, L. V. Johnson, R. Herrmann, S. Farsiu, S. G. Smith, M. Groelle, B. E. Mace, P. Sullivan, J. A. Jamison, U. Kelly, O. Harrabi, S. S. Bollini, J. Dilley, D. Kobayashi, B. Kuang, W. Li, J. Pons, J. C. Lin, and C. Rickman, "Anti-amyloid therapy protects against retinal pigmented epithelium damage and vision loss in a model of age-related macular degeneration," Proc. Natl. Acad. Sci. U.S.A. **108**(28), E279–E287 (2011).
8. H. Wu, X. Geng, X. Zhang, M. Qiu, K. Jiang, L. Tang, and J. Dong, "A self-adaptive distance regularized level set evolution method for optical disk segmentation," Biomed. Mater. Eng. **24**(6), 3199–3206 (2014).
9. P. Rangel-Fonseca, A. Gómez-Vieyra, D. Malacara-Hernández, M. C. Wilson, D. R. Williams, and E. A. Rossi, "Automated segmentation of retinal pigment epithelium cells in fluorescence adaptive optics images," J. Opt. Soc. Am. A **30**(12), 2595–2604 (2013).
10. K. Bredies, M. Wagner, C. Schubert, and P. Ahnelt, "Computer-assisted counting of retinal cells by automatic segmentation after TV denoising," BMC Ophthalmol. **13**(1), 59 (2013).

#242361 Received 8 Jun 2015; revised 20 Jul 2015; accepted 21 Jul 2015; published 23 Jul 2015

11. S. J. Chiu, Y. Lokhnygina, A. M. Dubis, A. Dubra, J. Carroll, J. A. Izatt, and S. Farsiu, "Automatic cone photoreceptor segmentation using graph theory and dynamic programming," Biomed. Opt. Express **4**(6), 924–937 (2013).
12. K. Devisetti, T. P. Karnowski, L. Giancardo, Y. Li, and E. Chaum, "Geographic atrophy segmentation in infrared and autofluorescent retina images using supervised learning," Conference proceedings: ... Annual International Conference of the IEEE Engineering in Medicine and Biology Society. IEEE Engineering in Medicine and Biology Society. Annual Conference 2011, 3958–3961 (2011).
13. S. J. Chiu, C. A. Toth, C. Bowes Rickman, J. A. Izatt, and S. Farsiu, "Automatic segmentation of closed-contour features in ophthalmic images using graph theory and dynamic programming," Biomed. Opt. Express **3**(5), 1127–1140 (2012).
14. E. Meijering, "Cell Segmentation: 50 Years Down the Road," IEEE Signal Process. Mag. **29**(5), 140–145 (2012).
15. A. Maeda, G. Palczewska, M. Golczak, H. Kohno, Z. Dong, T. Maeda, and K. Palczewski, "Two-photon microscopy reveals early rod photoreceptor cell damage in light-exposed mutant mice," Proc. Natl. Acad. Sci. U.S.A. **111**(14), E1428–E1437 (2014).
16. J. Kittler and J. Illingworth, "Minimum error thresholding," Pattern Recognit. **19**(1), 41–47 (1986).
17. A. A. Hill, P. LaPan, Y. Li, and S. Haney, "Impact of image segmentation on high-content screening data quality for SK-BR-3 cells," BMC Bioinformatics **8**(1), 340 (2007).
18. T. B. Tang, C. K. Lu, A. Laude, B. Dhillon, and A. F. Murray, "Noise reduction for ellipse fitting on medical images," Electron. Lett. **49**(3), 178–179 (2013).

Abbreviations

AMD, age-related macular dystrophy; RPE, retinal pigmented epithelium; SLO, scanning laser ophthalmoscope; TPM, two-photon fluorescence microscopy

1. Introduction

The structural and fluorescent properties of the retinal pigmented epithelium (RPE) cells in the retina are affected by several eye diseases such as age-related macular dystrophy (AMD) [1], glaucoma [2], and cone-rod dystrophy [3]. Two-photon fluorescence microscopy (TPM) allows non-invasive imaging of the RPE when paired with adaptive optics [4]. TPM can resolve and differentiate between retinosomes and damaging products of the visual cycle sequestered in the RPE [5]. Retinosomes contain retinyl esters, components of the retinoid cycle that restore visual pigments to their 'ready-to-be-activated' state. Both a lack of retinosomes and their increased dimensions could be indicative of a malfunctioning retinoid cycle as demonstrated by *Lrat*$^{-/-}$ and *Rpe65*$^{-/-}$ mice, respectively. To take advantage of the powerful capabilities of TPM, as with all imaging modalities, automated segmentation methods will be critical for analysis of imaging data sets [6].

If a structure is correctly segmented into its components, quantitative features of the structure such as area and density can be calculated [7]. Then, these features can be used to differentiate between healthy and diseased states [8, 9] and create a quantitative description of disease pathology [2].

Automated and quantitative processing of images have been developed for many features of the retina. For example, methods have been developed for identifying and segmenting: a) photoreceptor cells both labeled with immune-cytochemistry visualized microscopically and by adaptive optics ophthalmoscope [10, 11]; b) AMD and geographic atrophy from infrared and autofluorescent images [12]; c) increased fluorescent areas in the parapapillary region of glaucoma patients' retinas idenfied with a semiautomatic SLO (SLO) [2]; d) the optic disc with an ophthalmoscope [8]; and e) RPE cells with a fluorescent SLO [9]. Lastly, Chiu *et al* presented a method for segmenting RPE cells from confocal microscopy images [13].

However, none of these methods are directly applicable to segmentation of the RPE imaged by TPM. For example, only the cell borders of the RPE are visible when imaged by SLO. With TPM, more details about the cells are distinguishable including the retinosomes and nuclei. However, segmenting individual RPE cells is more challenging because the fluorescence of the borders is less distinguishable from that of the cell bodies, especially on a pixel by pixel basis, reducing the effectiveness of typical gradient- and intensity-based segmentation methods.

Many segmentation methods are based on histograms of image intensities [6]. Region growing is an alternative to edge based segmentation [14]. This strategy relies upon the

#242361 Received 8 Jun 2015; revised 20 Jul 2015; accepted 21 Jul 2015; published 23 Jul 2015
(C) 2015 OSA

features being sufficiently distinct to prevent accumulation of one region into another based on well-defined edges, intensity, and texture – attributes not found in TPM images of RPE.

Here, we present a semi-automated method for segmenting RPE cells imaged by TPM. The proposed method is designed to identify the border surrounding a nucleus within the image. It overcomes the weak signal of the cell border by two means. First, though the border is difficult to distinguish on a pixel by pixel basis, it can be identified over a region of pixels. Therefore, the method draws the cell border around a nucleus in segments. Second, the method employs a combination of gradient, intensity, and other features to determine the score of a border segment. In a 'greedy'-search, the method in turn selects those consecutive segments that score the best and are therefore the most likely to fall within the actual cell border. The only critical assumption our method makes about the structure of the image is that there is at least one nucleus per cell.

Testing on images collected from healthy retinas demonstrated that this method correctly identified individual RPE cells with up to 92% accuracy. In four images of aged retina, where the honey-comb structure of the RPE layer breaks down, the accuracy averaged 58%. Accuracy was determined in comparison to manually identified RPE cells, wherein a cell was considered correctly identified if the border encompassed the same nuclei within the cell as identified manually.

2. Methods

2.1 Implementation

All methods were implemented in the Ruby programming language in an object-oriented fashion. The software is freely available for academic institutions upon request. External libraries used included the RMagick library for reading in images and the Gnuplot library for writing images. The implementation takes about 1.6 minutes to run per nucleus in an image using an Amazon c3 compute node.

2.2 Mice

BALB/c and B6(Cg)-Tyr^{c-2J}/J mice were obtained from The Jackson Laboratory (Bar Harbor, Maine). All mice were housed in the animal facility at the School of Medicine, Case Western Reserve University, where they were maintained on a normal mouse chow diet in a 12 h light (~10 lux)/12 h dark cyclic environment. All animal procedures and experiments were approved by the Case Western Reserve University Animal Care Committees and conformed to both the recommendations of the American Veterinary Medical Association Panel on Euthanasia and the Association of Research for Vision and Ophthalmology.

2.3 Image collection

TPM images of BALB/c and B6(Cg)-Tyr^{c-2J}/J mice RPE were collected as previously described [15] using 730 nm excitation. Two images of four week old mice were collected with a resolution of 1024x1024. For analysis, they were down-sampled to 425x425 and contained 0.431 microns per pixel. Four images of two- and ten- month old mice were collected and analyzed with a resolution of 512x512, with each pixel representing 0.357 microns.

2.4 Nuclei segmentation with manual threshold selection

The minimum error threshold technique was used to segment nuclei from the background [16]. The number of histogram bins used for thresholding ranged between five and thirty (Fig. 6). From the resulting images, the best thresholded image was selected by visual inspection focused on minimizing noise without losing nuclei. Next, segmented pixel nuclei were set to negative-three times their original value to separate them from background and to retain nuclei pixels as prominent features during the next step which was to blur the image (Fig. 7(A)). Blurring was done by averaging the pixels in the 9x9 box of pixels surrounding each pixel (Fig. 7(B)). The final step was a second round of minimum error thresholding and again

#242361 Received 8 Jun 2015; revised 20 Jul 2015; accepted 21 Jul 2015; published 23 Jul 2015
(C) 2015 OSA

visually selecting the best image by reducing noise while leaving nuclei intact (Fig. 7(C)-7(E)). Lastly, for use in the next stage of segmenting the RPE cells, pixels selected as nuclei were set to an intensity of zero in the original image (Fig. 7(F)).

2.5 Nuclei segmentation with background correction, scored threshold selection, and noise filtering

To perform background correction and smooth the intensity over the image, the starting image (Fig. 8(A)) was first convolved with a 30x30 pixel kernel for uniformly averaging every pixel to create the background intensity image (Fig. 8(B)). Then the background intensity image was subtracted from the starting image to obtain the background corrected image (Fig. 8(C)), which brightens nuclei on the edges of the image relative to nuclei in the center of the image and makes the interior nuclei easier to segment (compare segmented nuclei of Fig. 1(A) and Fig. 1(B)).

The minimum error threshold finds the best intensity threshold for a given number of bins used to group the intensities, but the optimal number of bins must be determined such that the nuclei are best segmented while reducing noise. We propose a score to identify the best threshold image. First, thresholding was performed for a number of bins in the range between two and twenty four. Next, each of these thresholded images was scored. Because the thresholded images contained binary intensities of 0 or 1, the score was calculated as the sum of pixels with intensity of one, where an intensity of one indicates the pixel was thresholded as part of a nucleus. The rationale for this scoring scheme was that the best thresholded image has the smallest amount of pixels identified as nuclei, which also minimizes the amount of noise identified as nuclei. This strategy requires that the noise gets removed from foreground during thresholding more quickly than the nuclei pixels.

Using the background corrected image (Fig. 8(C)), we performed minimum error thresholding [16] for a number of bins in the range between two to fourteen. Each result was scored and the best threshold was selected by score (Fig. 8(D)). Then, the best thresholded image was subtracted from the original image (Fig. 9(A)) and blurred (Fig. 9(B)). The blurred image was then subjected to another round of minimum error thresholding with the number of bins ranging from ten to thirty.

At this point, all thresholded images were subjected to a filtering and scoring protocol taking into account the various features of groups of pixels that were thresholded as nuclei. The circularity of the nuclei was scored as follows. For every nucleus, the outer most pixels were selected. Then for every nucleus, the distance between the outer pixels and the center of the nucleus was calculated. The center was calculated as the mean of the pixel coordinates of the nucleus. This allowed an average distance between the center and the outer pixels as well as the standard deviation to be calculated for every nucleus. A circular nucleus will have a small standard deviation in the distance between the outer pixels and the center. The standard deviation of the radii was divided by the average radius to normalize the standard deviation to the radius size. This normalized standard deviation was used as the measure of circularity for each nucleus. Then, the average and standard deviation of circularity was calculated over all nuclei. Nuclei were kept as nuclei if their circularity was less than two standard deviations away from the average circularity.

A second measure of circularity was used that is sensitive to the area of the nucleus in relation to its circumference when compared to what is expected based on the radius. The radius was calculated as the average distance from outer pixels to the center pixel as described above. The area of the nucleus was determined by counting the number of pixels that comprised it. The circumference was determined by counting the number of edge pixels of the nucleus. An edge pixel is defined as any pixel where one of its 8 surrounding neighbors is not also a nucleus pixel. In practice, this meant any pixel with one of its eight neighbors that has an intensity greater than 0 is an edge pixel. The ratio between the area and circumference was calculated for every identified nucleus. The ratio of area to circumference is equal to 0.5 times the radius. To calculate the circularity of a nucleus, 0.5 times the radius was divided by the ratio of the area to circumference, which would give a value of one if the nucleus was

#242361 Received 8 Jun 2015; revised 20 Jul 2015; accepted 21 Jul 2015; published 23 Jul 2015
(C) 2015 OSA

perfectly circular. This circularity value was calculated for every nucleus, and the average and standard deviation were calculated over all nuclei. Every nucleus was then compared to the average circularity and considered a nucleus if its circularity deviated by a value less than 0.9 standard deviations from the average.

Lastly, nuclei were filtered by size to remove small noise patches. The average area of all nuclei was calculated along with the standard deviation. A nucleus was considered not a nucleus if its area was more than 1.5 standard deviations less than the mean.

Valid nuclei were those that met the three criteria given above. Next, a score for each thresholded image was calculated based on valid nuclei for that image. The score for an image was calculated as the number of valid nuclei in that image multiplied by the square root of the average area of the nuclei. This selected for thresholded images that have many nuclei that are large in size. The best image (Fig. 9(D)) was then combined with the original image as described by setting thresholded nuclei pixels within the original image to an intensity value of zero (Fig. 9(E), same as Fig. 1(B)).

To take advantage of the complementary performance of thresholding with and without background correction, the two resulting thresholded images were combined to form a unified nuclei threshold image. This has the advantage that both the nuclei in the center were robustly segmented as well as those in the edge regions. By combining the pixels identified as nuclei from the non-background corrected and background corrected images, the strengths of each result are shown in a single image (Fig. 1(C)). Filtering the combined image based on the three nuclei criteria described above removed any remaining noise from being identified as nuclei (Fig. 1(D)).

#242361 Received 8 Jun 2015; revised 20 Jul 2015; accepted 21 Jul 2015; published 23 Jul 2015
(C) 2015 OSA

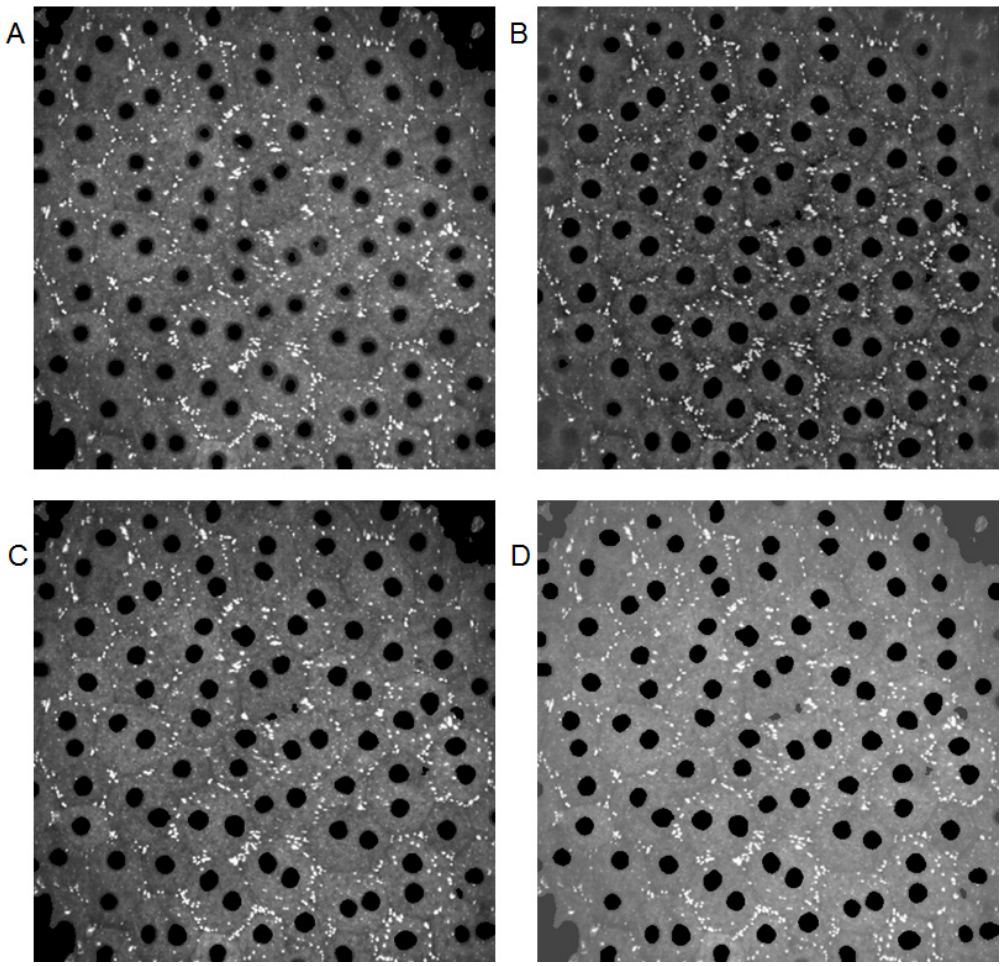

Fig. 1. Background correction improves nuclei segmentation when combined with non-background corrected nuclei segmentation. Pixels identified as being part of a nucleus are shown with zero intensity (black). A) Nuclei identified without background correction (same as Fig. 3(B) panel). B) Nuclei identified with background correction. C) The union of the pixels identified as nuclei from A) and B). D) Image from C) after noise filtering to remove false positive identification of nuclei pixels.

2.6 Input for RPE cell border identification

The images with nuclei segmented based on the manually selected thresholding protocol was used as the starting point for segmenting the cells (Fig. 2(A)). Intensity gradients within the image were calculated using the original image (non-thresholded nuclei) convoluted with the Sobel operator edge detector kernel (Fig. 2(B)). This Sobel gradient image along with the original image comprised the two inputs into the algorithm. Nuclei false positives and noise regions were filtered before cell segmentation. To filter noise, only the first described measure of circularity was used to validate nuclei. To summarize, this was accomplished by first calculating the average distance from edge pixels to the center of a nucleus, then calculating the average and standard deviation of the radius from those values and comparing the resulting mean normalized standard deviation to the average mean normalized standard deviation over all nuclei. A nucleus was considered valid and not noise if its circularity was within two standard deviations of the mean (Fig. 2(C)).

#242361 Received 8 Jun 2015; revised 20 Jul 2015; accepted 21 Jul 2015; published 23 Jul 2015
(C) 2015 OSA

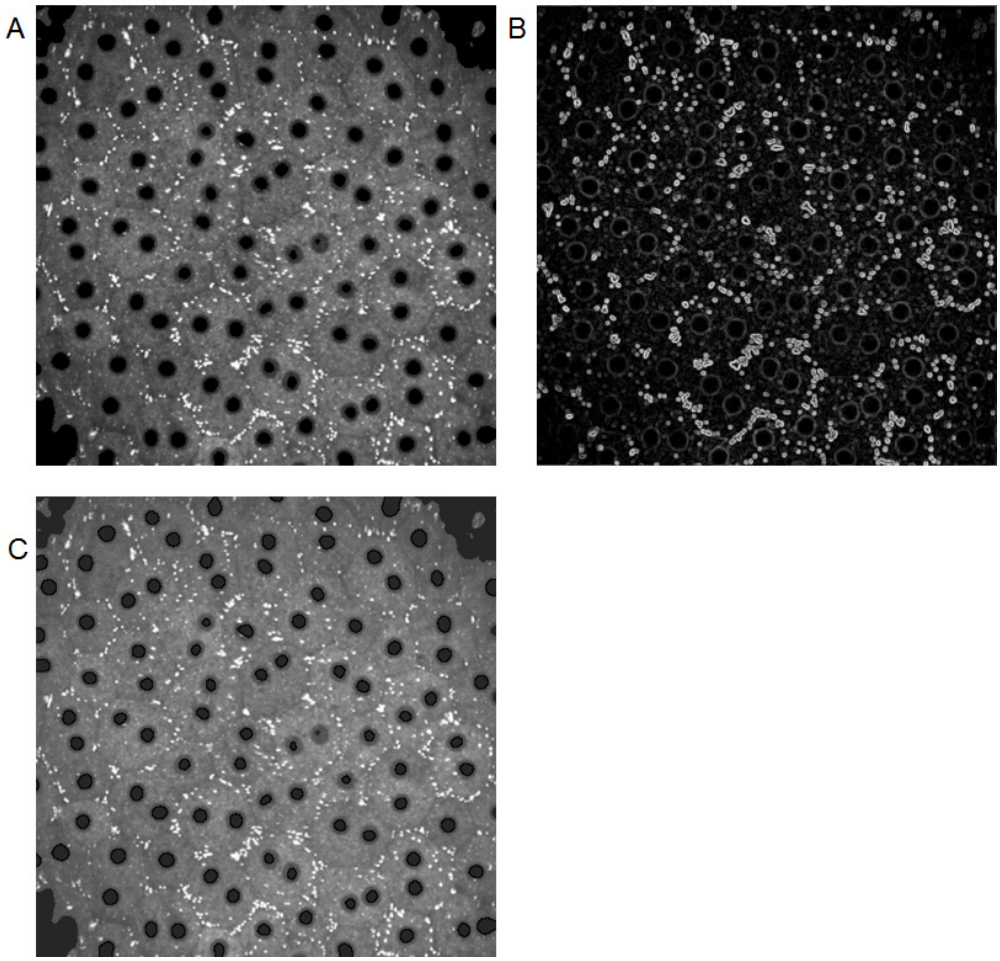

Fig. 2. Initial steps of the RPE cell segmentation process. Cell segmentation uses as input A) a segmented nuclei image (here, the same as Fig. 1 A panel) and input B) the gradient image as calculated using the Sobel operator on the original image. C) The first step is to filter out noise segmented as nuclei. Accepted nuclei are shown with dark black outline. For an overview of the full process, see Visualization 1, Visualization 2, and Visualization 3 for demonstrations of drawing the searching segments, drawing the border, and assigning pixels to a cell, respectively.

2.7 RPE cell border identification

The general strategy of our method was to identify the border around a nucleus using multiple weak scoring functions. The cell border around each nucleus was determined independently in an image. First, the searchable border region was limited to a region not too far and not too close to the current nucleus of interest. We used a minimum distance of ten pixels and a maximum distance of sixty-four pixels within which a border could be identified (Fig. 10(A)). Pixels around the nucleus were grouped into angles of 21 degrees, starting at the upper left most pixel of the nucleus (Fig. 10(B)). Boundaries were not repeated; the final wedge has three degrees to complete the full 360 circle. The upper-left-most pixel was used as an anchor point for defining the angle around the nucleus and considered zero degrees, with the center of the nucleus always being the middle vertex. The starting seed for the cell border was selected from the wedge of pixels between ten and sixty-four pixels away from the nucleus between zero and 21 degrees (Fig. 10(C)). The starting seed was selected by scoring all pixels within the wedge and taking the pixel with the best overall score. Four scores were used.

#242361 Received 8 Jun 2015; revised 20 Jul 2015; accepted 21 Jul 2015; published 23 Jul 2015
(C) 2015 OSA

Moreover, these scores are also used to score the line segments of pixels being tried as candidates for the border edges (see below).

a) Gradient Score: The average gradient value for a pixel or a set of pixels as calculated by the Sobel operator. This works under the assumption that larger gradients will occur at cell borders. Score was weighted by –0.0015 during seed-pixel selection.

b) Nuclei Distance Score: For a single pixel or a set of pixels, the shortest distance from any of those pixels to any nuclei. This works under the assumption that border pixels are more frequently further away rather than closer to any nucleus. Score was weighted by –4000 during seed-pixel selection.

c) Nucleus of Interest Closeness Score: This score uses two sets of pixels. The first set is all the pixels of the nucleus which is currently having its border determined. The second set of pixels can be an individual pixel or a set of pixels – for example, a border edge. The distance from each pixel in the first set to each pixel in the second set is measured in number of pixels. The score is the largest measured distance between these two sets of pixels. This works under the assumption that the border around the nucleus of interest will be closer to the nucleus rather than farther away from it. Score was weighted by 6.0 during seed-pixel selection.

d) Intensity Score: First, pixels determined to be part of retinosomes were excluded from this calculation. Retinosomes were identified by thresholding the image; any pixels with intensities more than 1.75 standard deviations greater than the image mean were considered part of a retinosome. This threshold was selected because it performed satisfactorily upon visual inspection. With this information, the average intensity of a pixel or set of pixels was calculated. Any pixels considered part of a retinosome were excluded from the calculation of the mean. This works under the assumption that border pixels will have low intensities. Score was weighted by 0.012 during seed-pixel selection.

If there were no eligible pixels (for example due to the edge of the image) within the initial wedge, the search for the starting pixel was moved to the next 21 degree wedge and this continued until a wedge with at least one eligible pixel was found.

With the border starting pixel identified, we then searched for the border's first edge. This was accomplished by getting all the pixels in the neighboring wedge in a counter-clockwise direction, and scoring the edge formed between each pixel and the starting pixel (Fig. 10(D)). The trial edges then were scored using the same four scores: the Gradient Score (weight: –0.0015), Nuclei Distance Score (weight: square root of Nuclei Distance Score multiplied by –990.0), Nuclei of Interest Closeness Score (weight: 4.0), and Intensity Score (weight: 0.0240). The edge with the best score was selected. The next 21 degree bin of pixels was also checked to find if it offered a better edge than could be created from the first neighboring 21 degree wedge. Once the best edge was selected, the process of building up the border continued around the nucleus of interest (Visualization 1). If the boundary of the image was encountered, the process resumed at the furthest vertex in the clockwise direction, and continued edge building in a clockwise direction. Once edges were determined around all angles, the starting pixel was linearly connected to the ending pixel.

Edges were formed between non-adjacent pixels by using linear interpolation of the rows and columns over the distance between them to connect them. First, the distance between the two non-adjacent pixels was calculated. One of the pixels was arbitrarily selected as the starting pixel. The distance was linearly divided into distance + 1 steps to connect the two pixels. The row and coordinates of subsequent pixels were determined by Eq. (1) and Eq. (2).

#242361 Received 8 Jun 2015; revised 20 Jul 2015; accepted 21 Jul 2015; published 23 Jul 2015
(C) 2015 OSA

$$row = row_start + \left(dist_fraction * \left(row_end - row_start\right)\right). \quad (1)$$

$$col = col_start + \left(dist_fraction * \left(col_end - col_start\right)\right). \quad (2)$$

where the *distance_fraction* is the current step divided by the distance, *row_start* and *col_start* are the coordinates of the starting pixel, and *row_end* and *col_end* are the coordinates of the ending pixel.

Six independent trials identifying each cell border were conducted. With each trial, the starting seed began within a new angle range at a new position around the nucleus, specifically sixty degrees away from the previous starting seed position (Visualization 2). After each independent trial, the border determined for that trial was scored. Seven scores were used, three of which are described above: Gradient Score (weight: −0.0015), Intensity Score (weight: 0.024), Nuclei Distance Score (weight: square root of Nuclei Distance Score multiplied by −50.0). The other four scores are described below.

e) Fraction of Pixels on Image Boundary Score: This score provided the fraction of pixels within a determined cell border that fell on the edge of the image. The assumption of this score was that if most of the pixels comprising a border fall on the edge of the image, the pixels cannot properly be circling a nucleus. The score was weighted as score squared multiplied by 500.

f) Border Size Score: The value of this score is the number of pixels that comprise a border. This selects for a larger rather than smaller border size. The score was weighted as one-third root of the score multiplied by −20.

g) Boundary Relative to Nucleus Score: First, the circumference of the nucleus for an ideal circle based on the area of the nucleus was calculated. Given the area as the number of pixels that make up the nucleus, the radius was calculated as if the nucleus were a perfect circle. From this radius, the circumference of the nucleus then was calculated. The score was the ratio of the nucleus circumference to the border size. The border size was the number of pixels comprising the border. If the ratio was larger than one, a penalty was assigned to that border because it means the circumference of the nucleus is larger than the circumference of the determined border of the cell. This score was weighted by 1000.

h) Border on Nuclei Score: This score compared the coordinates of a border to the coordinates of all nuclei within the search region, and gave the number of pixels that overlap between these two sets. The assumption of this score is that the border should not pass through a nucleus. The value was weighted by 100.

The border with the best overall score was selected as the border for the cell around the current nucleus of interest. The process was repeated for every nucleus identified in the image. In the end, a cell border was determined for every valid nucleus.

The next step was to assign the pixels within a cell border to a nucleus, which allowed the cell to be identified based on both its pixels and nucleus (or nuclei if there was more than one nucleus). Collecting pixels belonging within a cell for a given nucleus was accomplished by collecting pixels starting at the center of a nucleus and growing outward until border pixels were encountered (Visualization 3). If more than one nucleus resided within a border, and the border for each nucleus contained the center of the other nucleus, both nuclei were considered to lie within the same cell. Inconsistencies were resolved by keeping both scenarios. For example, if there are two nuclei, the border of the first contains both nuclei, and the border of the second contains only the second nucleus, then they were considered to be two cells: one with both nuclei and one with only the second nucleus.

#242361 Received 8 Jun 2015; revised 20 Jul 2015; accepted 21 Jul 2015; published 23 Jul 2015

2.8 RPE cell border identification with revision

After cells were determined by the pixels and nuclei that made them up, a process was implemented to improve the border around a nucleus, *n*. This approach took advantage of the fact that there are frequently multiple nuclei within a cell and therefore multiple borders should be available to define the boundary of that cell. In the event that imaging is carried out where multiple nuclei are not expected, the same effect can be achieved by running the initial border determining protocol more than once and collecting the resulting borders for each nucleus. The revision protocol for a given cell, *c*, containing *n* was as follows, assuming that all nuclei that are contained within the border of *c* are identified, and all nuclei in cells with borders containing the nuclei of *c* are identified. Scores of the borders for all of these identified nuclei were compared to one another. The best scoring border was used to identify which cell *n* belonged to, taking into account three possible scenarios. First, *n* belongs to the cell in which it was originally identified. In this case, the cell originally identified to contain *n* stays as it was originally determined. Second, *n* belongs to another cell whose border contains *n* but the border of *n* does not encompass the same region. Here, the border of *n* is changed to be the border of the other cell, and *n* belongs to a new cell along with any other nuclei within that other cell. In the third possible scenario, the best border is derived from a nucleus whose border does not contain *n*. In this case, *n* cannot be in cells whose nuclear composition matches that of the cell with the best scoring border. So, those cells are removed as candidate cells for *n*, and, out of the remaining cells, the best scoring border is taken as the best border for *n*. The result of one of these three scenarios was used to define the revised borders.

Using the revised nuclei and border assignments, the method made the final determination of border and nuclei comprising a cell. The nucleus border assigned to cell *c* was determined by taking the assigned revised border according to the nucleus that cell's border was derived from and recursively continuing until it reached a nucleus which was assigned to its original border. This then was the border used for the cell. This process resulted in a single border for a cell, even if there were multiple nuclei within it.

3. Results

3.1 Nuclei Segmentation with manual threshold selection

We were able to segment all visible nuclei for the six images (Fig. 3). Although the area of each of the nuclei was not entirely recovered, this was not needed to determine the cell border by our method. As the images became noisier, false positive nuclei also were evident (e.g. Figure 3(F)). At the corners of these images, regions of noise were segmented as nuclei.

#242361 Received 8 Jun 2015; revised 20 Jul 2015; accepted 21 Jul 2015; published 23 Jul 2015
(C) 2015 OSA

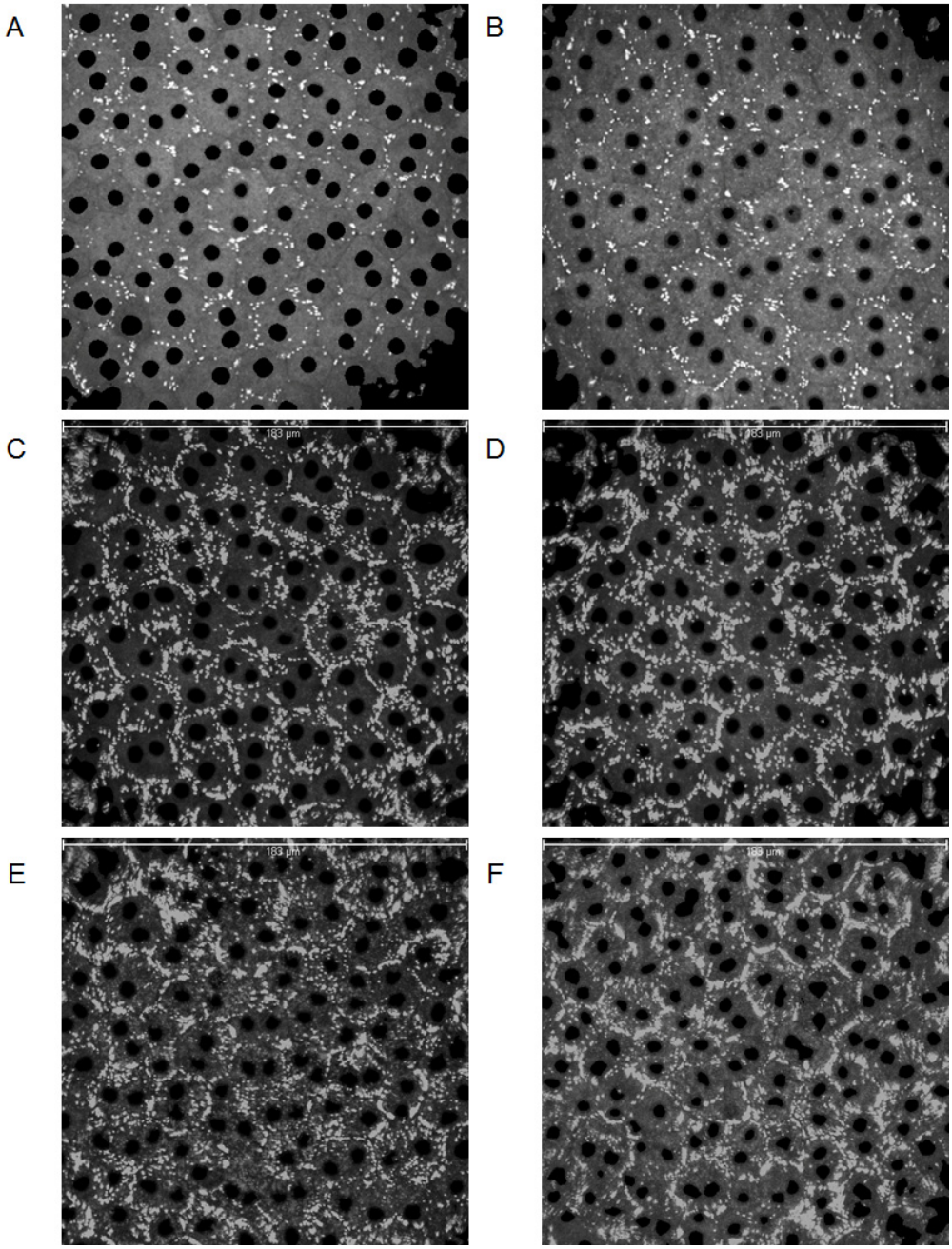

Fig. 3. Resulting identified nuclei after manually selected thresholding process. The pixels identified as being part of a nucleus are shown with zero intensity (black). A-B) 4-week-old BALB/c mice C-D) 2-month-old B6(Cg)-Tyr^{c-2J}/J mice E-F) 10-month-old B6(Cg)-Tyr^{c-2J}/J mice

3.2 RPE cell border identification

The success of drawing a border around each nucleus was considered separately for each nucleus, even if two nuclei appeared to be within the same cell. So, the number of possible successes was equal to the number of identified nuclei. A border was considered successfully

#242361 Received 8 Jun 2015; revised 20 Jul 2015; accepted 21 Jul 2015; published 23 Jul 2015
(C) 2015 OSA

identified if it exactly encompassed the nuclei that fell within its related cell, as determined by manual inspection. Over the six images obtained, the average success rate was 69% (Table 1). However, there was a large disparity between images. Two of the images had a success rate of 92% and 89% (Visualization 4 and Visualization 5, respectively), while the other four images had an average success rate of 58% (Visualization 6, Visualization 7, Visualization 8, and Visualization 9). Borders considered successes, borders considered failures, and any borders excluded from counts of success and failures are shown for each image in Visualization 4, Visualization 5, Visualization 6, Visualization 7, Visualization 8, and Visualization 9 A-C, respectively. The two best segmented images had the smallest amount of retinosomes (Fig. 4(A), 4(B)). Cell bodies in the other four images were not as prominent because of the amount of retinosomes and loss of the normal RPE structure (Fig. 4(C)-4(F)).

Table 1. Success rate of identifying RPE borders over six images[a].

image	age	type	successes	fails	total	% success
a	4-week-old	BALB/c	95	8	103	92
b[b]	4-week-old	BALB/c	85	10	95	89
c	2-month-old	*B6(Cg)-Tyr^{c-2J}/J*	61	35	96	64
d	2-month-old	*B6(Cg)-Tyr^{c-2J}/J*	52	36	88	59
e	10-month-old	*B6(Cg)-Tyr^{c-2J}/J*	65	41	106	61
f	10-month-old	*B6(Cg)-Tyr^{c-2J}/J*	59	61	120	49

[a]see Visualization 4, Visualization 5, Visualization 6, Visualization 7, Visualization 8, and Visualization 9 for which category every border was classified as
[b]Image from [15].

#242361 Received 8 Jun 2015; revised 20 Jul 2015; accepted 21 Jul 2015; published 23 Jul 2015
(C) 2015 OSA

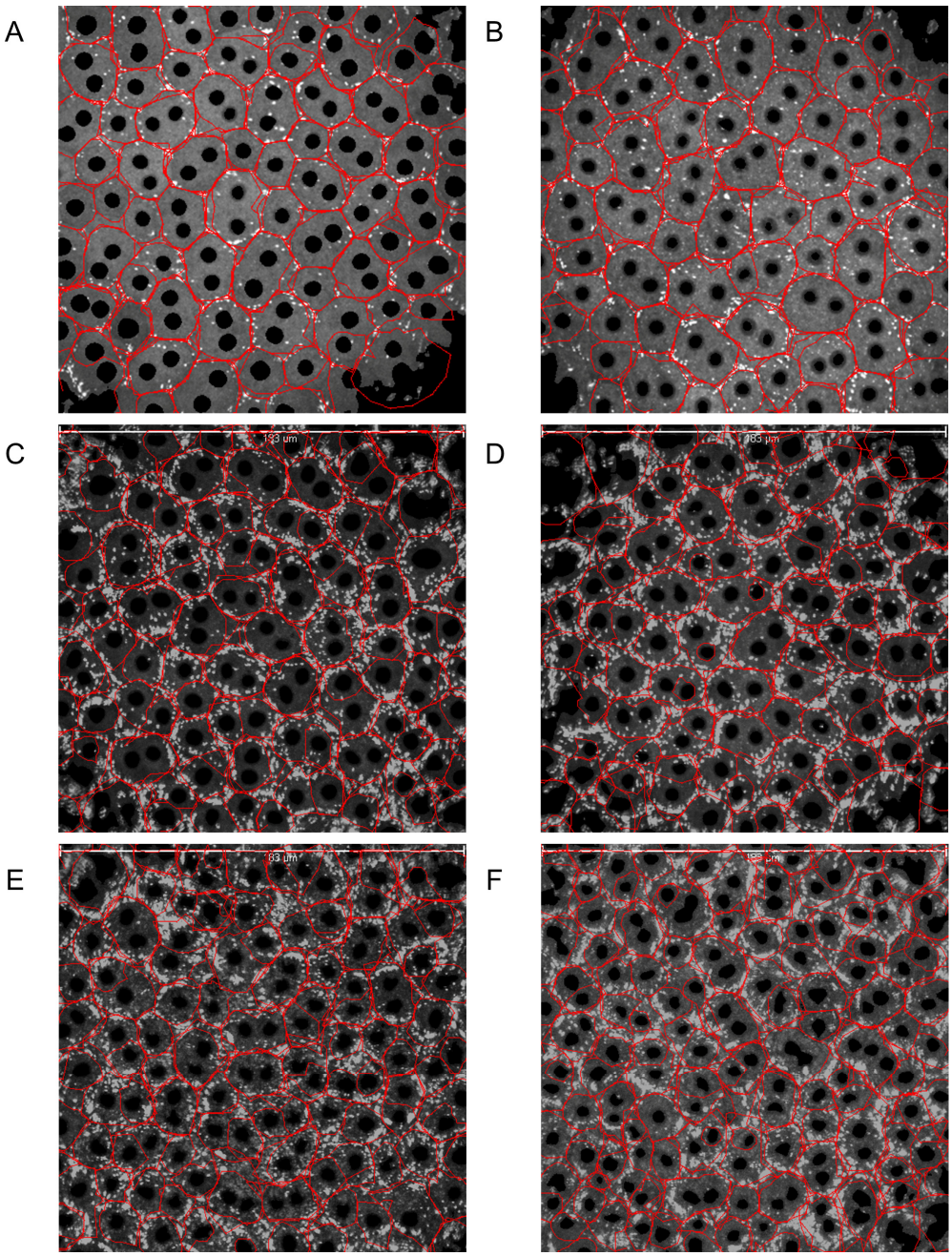

Fig. 4. Segmentation of RPE cells in six images of mice collected by TPM. Identified borders are shown as red lines around nuclei. A, B) Images collected from 4-week-old BALB/c mice corresponding to *a* and *b* in Table 1, respectively. Visualization 4 and Visualization 5 show which borders are considered successes, failures, and ignored from analysis for panels A and B, respectively. C, D) Images collected from 2-month-old B6(Cg)-Tyr^{c-2J}/J mice corresponding to *c* and *d* in Table 1, respectively. Visualization 6 and Visualization 7 show which borders are considered successes, failures, and ignored from analysis for panels C and D, respectively. E, F) Images collected from 10-month-old B6(Cg)-Tyr^{c-2J}/J mice corresponding to *e* and *f* in Table 1, respectively. Visualization 8 and Visualization 9 show which borders are considered successes, failures, and ignored from analysis for panels E and F, respectively.

#242361 Received 8 Jun 2015; revised 20 Jul 2015; accepted 21 Jul 2015; published 23 Jul 2015
(C) 2015 OSA

3.3 RPE cell border identification with revision

Using the initial RPE cell segmentation results, we then tested to see if our scheme for revising the borders could improve the success rate. For images *c-f* in Table 1 and, correspondingly, Fig. 4(C)-4(F), the revision process provides an improvement in accuracy for each image, but the improved average accuracy across the four images is still only 68% (Table 2). We attribute this to the high retinosome content and poorly resolved cellular structures in these images. However, for the two images which were initially most successfully segmented, revising the cell borders further improved the success rate to 95% of border identification (Table 2). The failure rate was reduced from eight and ten down to five for each image, representing an improvement in the failure rate of 37% and 50%, respectively. There were two types of failures successfully rectified. The first type was when the determined cell border around a nucleus encompasses fewer nuclei and creates a smaller cell than it truly should – for example, a single nucleus instead of a two-nucleus cell. If the cell border around the neighboring nucleus correctly encompasses both nuclei, then the border around the first, incorrectly determined small cell could be inside the larger cell border (Fig. 5(A)). Here, the neighboring nucleus' border was correctly identified as the better border during the revision process (Fig. 5(B)). The second type of failure was when the border around a nucleus encompassed too many other nuclei (Fig. 5(C), 5(E)). After considering the scores of the other nuclei involved in the disputed border, the correct border was selected (Fig. 5(D), 5(F)).

Table 2. Success rate of identifying RPE cell borders after revision of the borders.

image	age	type	successes	fails	total	% success
a	4-week-old	BALB/c	98	5	103	95
b[a]	4-week-old	BALB/c	90	5	95	95
c	2-month-old	*B6(Cg)-Tyr^{c-2J}/J*	74	22	96	77
d	2-month-old	*B6(Cg)-Tyr^{c-2J}/J*	63	25	88	72
e	10-month-old	*B6(Cg)-Tyr^{c-2J}/J*	68	38	106	64
f	10-month-old	*B6(Cg)-Tyr^{c-2J}/J*	71	49	120	59

[a]Image from [15].

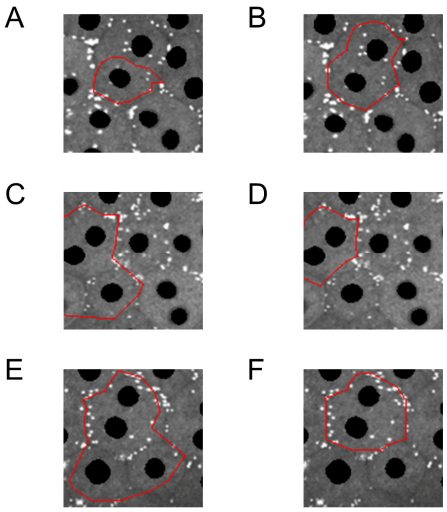

Fig. 5. Examples of three successful corrections of cell borders determined for nuclei in image *a* of a 4-week-old BALB/c mouse. The left images (A, C, E) show the border around a nucleus as initially determined. The right images (B, D, F) show the border around the corresponding nucleus (A, C, E, respectively) after revising the border as described in text. Borders are shown as red lines; pixels identified as nucleus are shown as black.

#242361 Received 8 Jun 2015; revised 20 Jul 2015; accepted 21 Jul 2015; published 23 Jul 2015

4. Discussion

To our best knowledge, semi-automated segmentation of RPE cells from TPM images of the retina has not previously been reported. So how does the performance of our method compare to that of other methods for segmenting structures within the retina?

Bredies *et al*. [10] accurately identified 93% of their manually identified photoreceptor cells, whereas Chiu *et al*. [11] identified 99% of photoreceptors with a false positive rate of 1.5%. Chiu at al [13]. also used a set of scores to help define the RPE borders and connect edges between pixels based on these scores. However, their images were from confocal microscopy. On average, Chiu *et al*. [13] segmented cells with an error of 1.49% in the number of cells segmented versus the number actually found in the image. On a per-pixel basis of segmenting geographic atrophy, Devisetti *et al*. [12] achieved a specificity of 92.9%. Segmenting retinal images from fluorescent SLO resulted in missing an average of 19 / 206 cells or a 91% success rate; on simulated noisy data, this method achieved a success rate of 97.21% [9]. Our current method does not reach the accuracy of the aforementioned algorithms but provides a baseline for comparison as the TPM field matures and analysis of TPM images advances. Our method employed several steps to arrive at the final segmentation result. This is common for segmentation methods, including segmentation of the RPE by fluorescent SLO [9].

On images of retinosome-rich retina, the accuracy of our method in identifying cell borders decreased. This was accompanied by a corresponding decrease in the visible presence of cell borders, as structures of the RPE cells began to break down. A high density of retinosomes in cell images is an important feature indicative of early disease that can easily be segmented. Thus, the amount of retinosomes could be used to inform an algorithm as to the status of the expected disease state and therefore the expected integrity of the RPE mosaic. Retinosome content possibly could also be employed to adjust the scoring functions and improve segmenting cells in diseased states, by using retinosomes as expected points along the cell borders, where they usually sequester [5]. Additionally, for individuals with increased retinosome content, an image of RPE could be collected at a longer excitation wavelength, thereby de-emphasizing retinosome visibility. It remains an important open question to quantitatively evaluate retinosome characteristics to determine if specific distributions or morphologies are indicative of different disease states. In addition, such studies will allow improved scoring schemes for future segmentation methods. There is a trend of increased disparity in the accuracy of images taken from mice of the same age and genotype, as the age of the mice increases. We attribute the disparity to normal variation within RPE; as the health deteriorates and the retinosome content increases, the possibility for larger variation in the RPE structure also increases, making segmentation less consistent.

Our images were taken of mice wherein most RPE cells contained two nuclei. But RPE cells of humans only contain a single nucleus under normal conditions. However, our method should still be applicable to humans, as it can correctly identify the border around RPE cells that have at least one nucleus.

Many studies rely on quantification of imaged structures but their conclusions are only valid if the segmentation is accurate [17]. The ability to segment cells is directly related to the gradients associated with the demarcating edges [18], especially as demonstrated with cell fluorescence images [6]. In TPM of RPE cells, the small difference in intensity between the cell bodies and their borders makes proper segmentation a difficult but feasible task as we demonstrate here. The accuracy of the current method is measured at the resolution-level of encompassing the correct nuclei belonging to a cell. As a result, any determined cell border pixel or edge around a nucleus may not precisely track the true cell border. Because each border is determined individually, gaps and overlaps occur between borders of adjacent cells. To approach border identification with per-pixel accuracy, future methods could refine borders taking into account neighboring cells. If desired, our method could be used in conjunction with additional segmenting procedures such as active contouring to further refine

#242361 Received 8 Jun 2015; revised 20 Jul 2015; accepted 21 Jul 2015; published 23 Jul 2015
(C) 2015 OSA

the placement of cell borders, after using the results from our method as the initial placement of the contour [8].

Six images were used to validate and test the algorihm of our successful segmentation of RPE cells imaged with TPM. Ideally, a separate and larger data set would have been used for validation and testing purposes. However, no specific features relating to the images were used in the development of the algorithm. Scores were based only on general observations about the overall structure of RPE images obtained by TPM. Multiple scores were used to determine an overall optimal border for each nucleus. Although each score by itself did not suffice to correctly determine cell borders, the interplay between them allowed a reasonable border to be determined. We suggest that, as larger and more diverse data sets become available for testing, the method will be generally applicable as TPM becomes a more commonly used imaging modality.

Appendix 1 figures

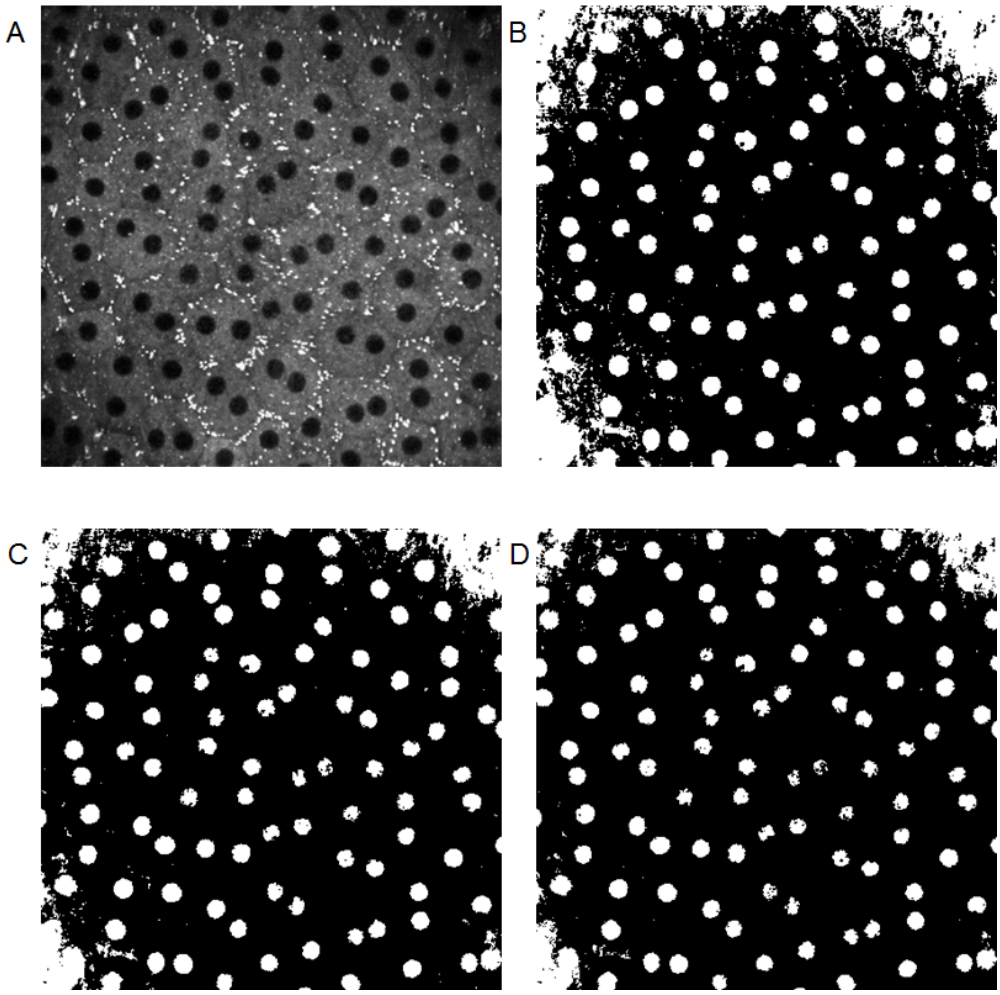

Fig. 6. Kittler minimal error thresholding applied to a TPM RPE image. A) Starting image of 4-week-old BALB/c mouse. B-D) Thresholded images with nuclei identified as white pixels. Number of intensity bins is 10, 12, and 14 in B, C, and D, respectively.

#242361 Received 8 Jun 2015; revised 20 Jul 2015; accepted 21 Jul 2015; published 23 Jul 2015
(C) 2015 OSA

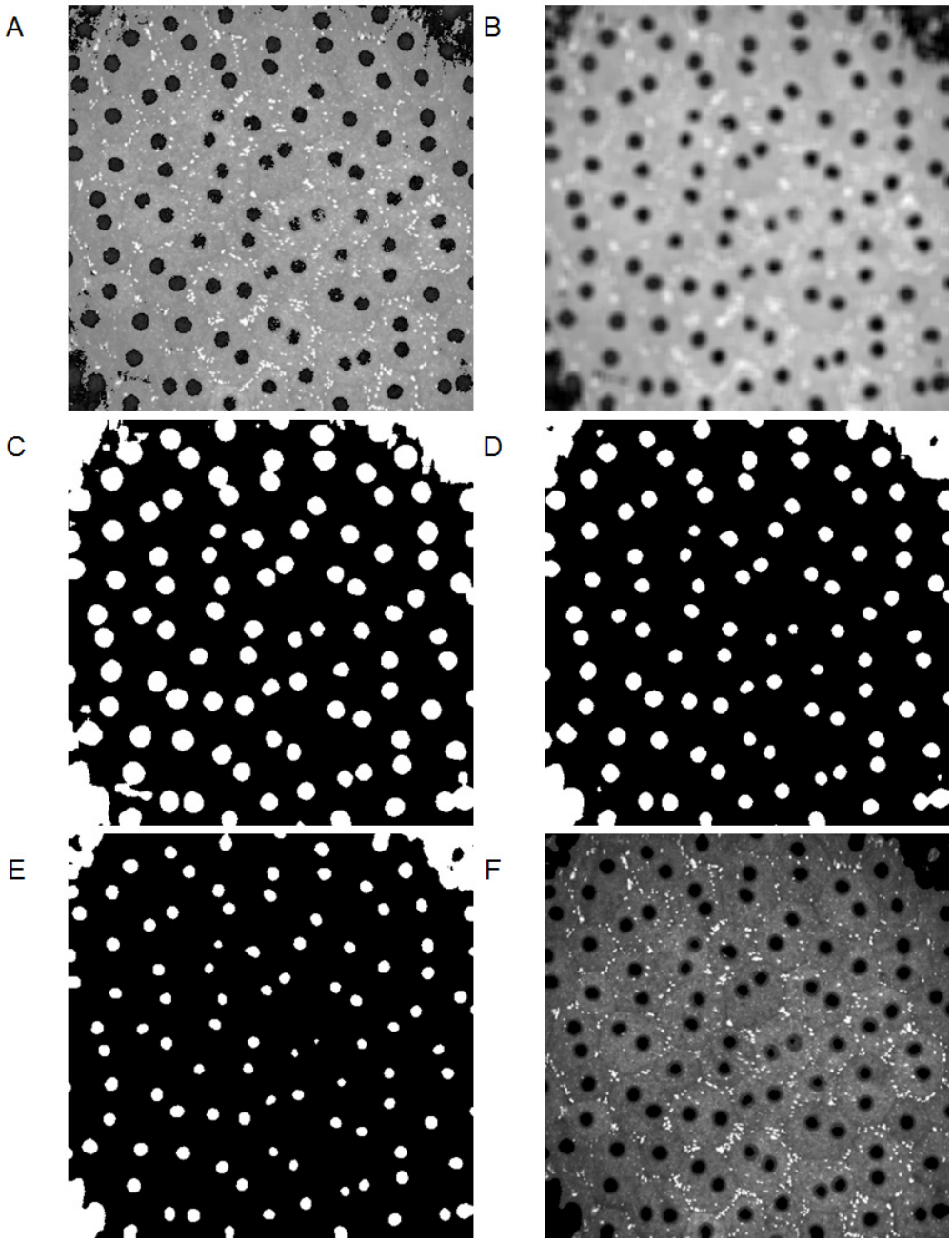

Fig. 7. Continued from Fig. 6, the process of segmenting the nuclei. A) After selecting the best thresholded image, the selected nuclei pixels are set to low intensity values on the original image. B) The image pixels are then averaged with the 9x9 box of pixels around each pixel. C-E) The blurred image (panel B) is then subjected to a second round of Kittler minimum error thresholding: the number of intensity bins here is 3, 4, and 6 for C, D, and E respectively. F) The pixels which are identified as belonging to a nucleus after the second round of thresholding are set to zero intensity.

#242361 Received 8 Jun 2015; revised 20 Jul 2015; accepted 21 Jul 2015; published 23 Jul 2015
(C) 2015 OSA

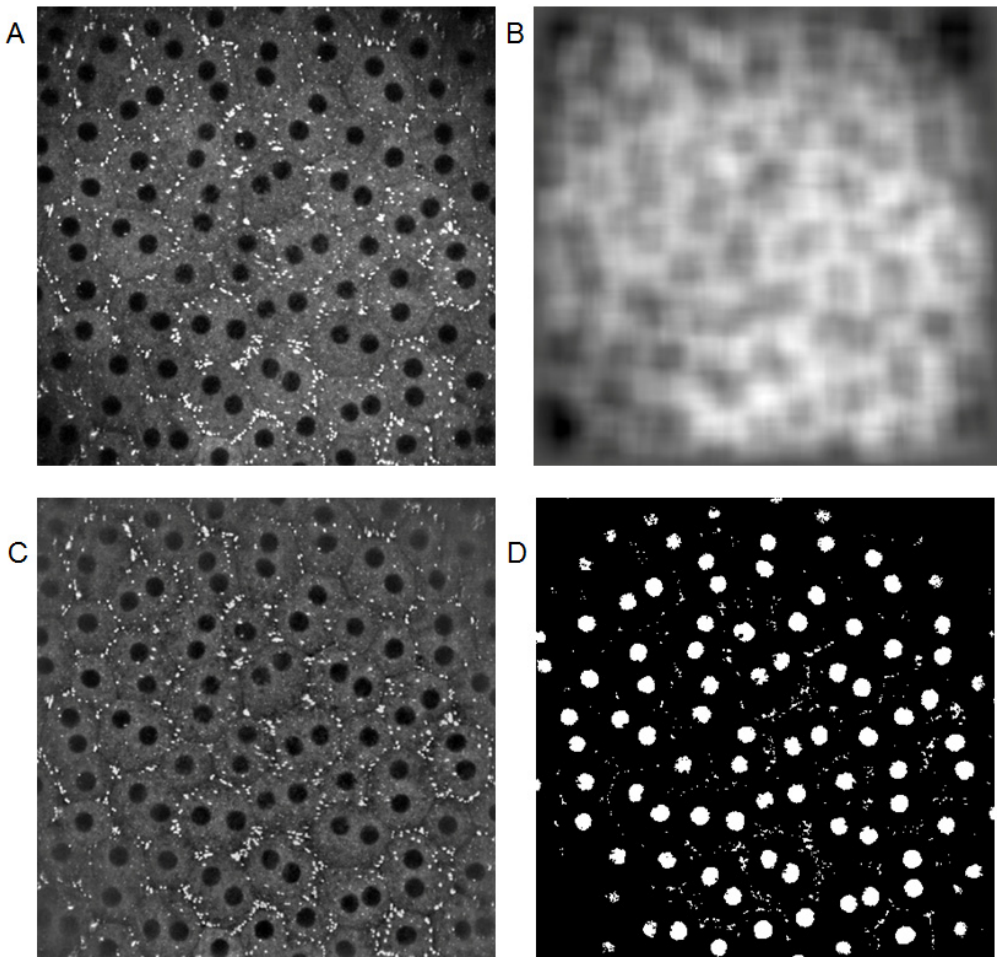

Fig. 8. Nuclei segmentation using background intensity correction and scored minimum error thresholding. A) The starting image (same as Fig. 6 A) of a 4-week-old BALB/c mouse RPE. B) The background illumination pattern. C) The original image (panel A) after subtracting the background illumination pattern. D) The best image which was selected by score after the image from C) was subjected to Kittler minimum error thresholding with multiple numbers of bins, as described in the text.

#242361 Received 8 Jun 2015; revised 20 Jul 2015; accepted 21 Jul 2015; published 23 Jul 2015
(C) 2015 OSA

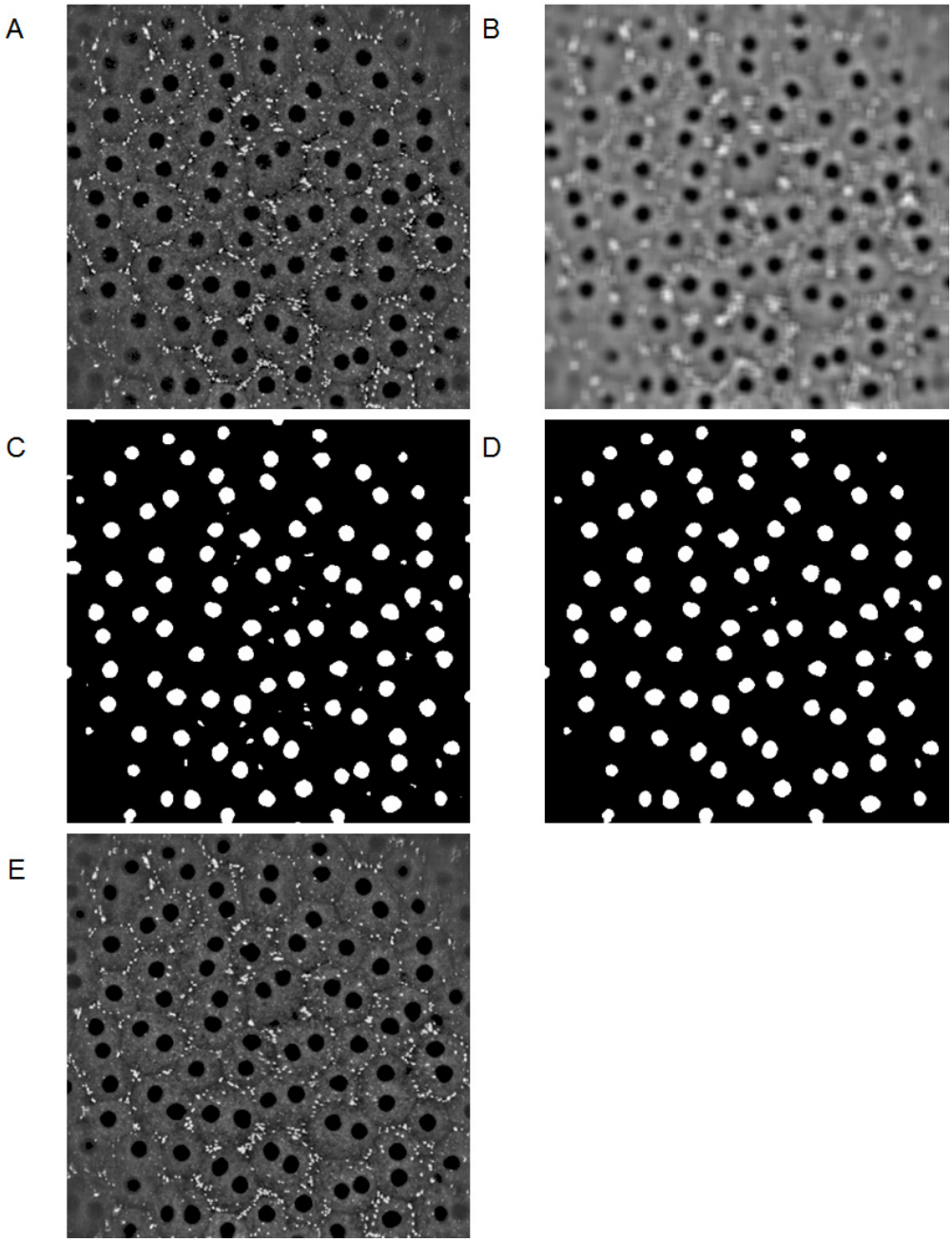

Fig. 9. Continued from Fig. 8 the second round of thresholding on the background corrected image with noise filtering. A) Starting image after first round of thresholding. Nuclei are identified by black pixels. B) Image from panel A) after the pixels are averaged using the 9x9 set of pixels surrounding each pixel. C) Best image before filtering. D) Best image after filtering noise as described in the text. E) The original background corrected image with determined nuclei pixels set to intensity zero (black).

#242361 Received 8 Jun 2015; revised 20 Jul 2015; accepted 21 Jul 2015; published 23 Jul 2015
(C) 2015 OSA

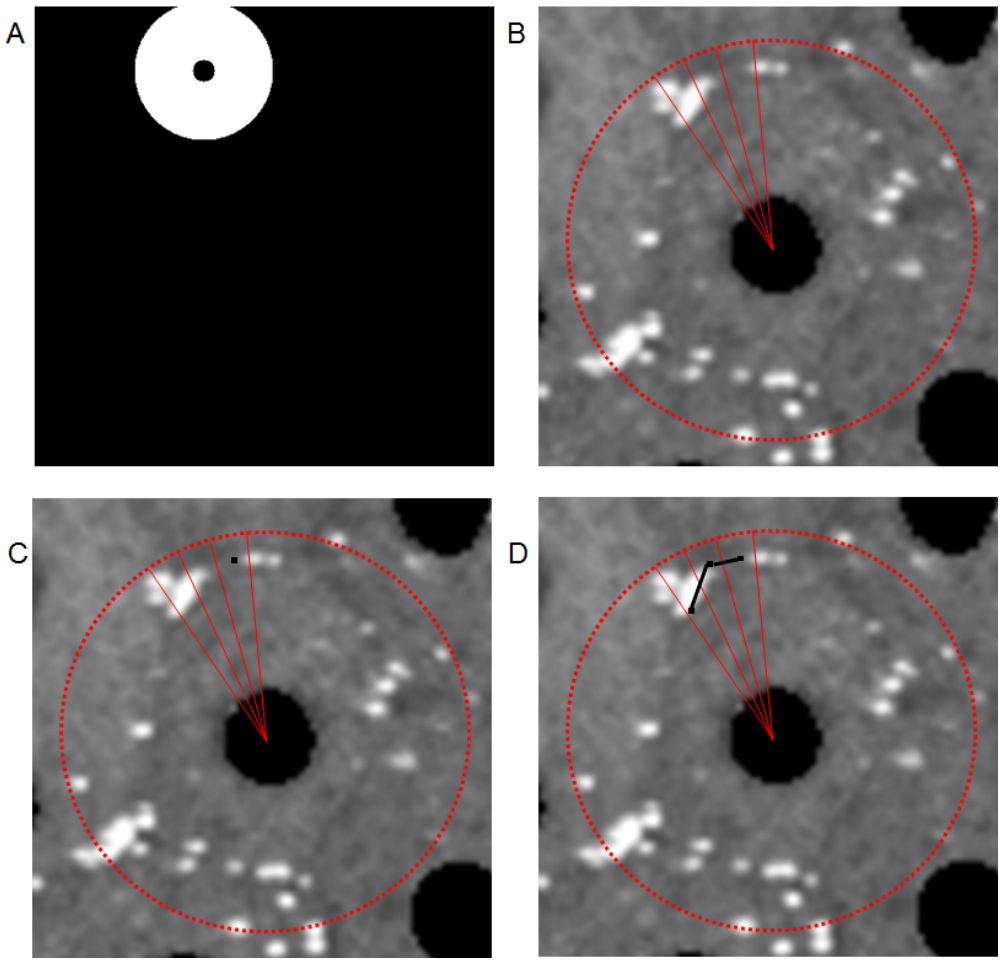

Fig. 10. Initial stages of drawing a border. A) An eligible search region is defined with pixels that could be used to form the border, shown in white. B) Pixels are grouped into wedges of 21 degrees, starting at the upper left most pixel of the nucleus. Each wedge contains the pixels eligible to be vertices for edges. C) All pixels within the first wedge are scored and the pixel with the best score is selected. D) The border is continued by sampling nuclei from the next neighboring wedge, scoring all possible edges, selecting the best scoring edge, and repeating this process around the nucleus. See Visualization 1, Visualization 2, and Visualization 3 for demonstrations of drawing the searching segments, drawing the border, and assigning pixels to a cell, respectively.

Appendix 2 visualizations

Visualization 1. "Greedy" edge search optimization. Starting from an initial edge vertex, edges to pixels in the neighboring two twenty-one degree wedge regions (see Fig. 10) are scored, and the best is selected for that edge segment. The process continues in a counter clockwise direction.

Visualization 2. Six independent trials are conducted for drawing the cell border around the nucleus. Each trial starts sixty degrees counter-clockwise around from where the previous trial started. The border is shown as black lines.

Visualization 3. Assigning cell pixels and nucleus (or nuclei) to an RPE cell. The pixels identified as belonging to the cell are shown in black.

#242361 Received 8 Jun 2015; revised 20 Jul 2015; accepted 21 Jul 2015; published 23 Jul 2015
(C) 2015 OSA

Visualization 4. For the TPM RPE image *a* from Table 1 of a 4-week-old BALB/c mouse, designation of which borders were considered A) successes, B) failures, and C) were excluded from consideration.

Visualization 5. For the TPM RPE image *b* from Table 1 of a 4-week-old BALB/c mouse, designation of which borders were considered A) successes, or B) failures. No borders were excluded from consideration.

Visualization 6. For the TPM RPE image *c* from Table 1 of a 2-month-old B6(Cg)-Tyrc-2J/J mouse, designation of which borders were considered A) successes, B) failures, and C) were excluded from consideration.

Visualization 7. For the TPM RPE image *d* from Table 1 of a 2-month-old B6(Cg)-Tyrc-2J/J mouse, designation of which borders were considered A) successes, B) failures, and C) were excluded from consideration.

Visualization 8. For the TPM RPE image *e* from Table 1 of a 10-month-old B6(Cg)-Tyrc-2J/J mouse, designation of which borders were considered A) successes, B) failures, and C) were excluded from consideration.

Visualization 9. For the TPM RPE image *f* from Table 1 of a 10-month-old B6(Cg)-Tyrc-2J/J mouse, designation of which borders were considered A) successes, B) failures, and C) were excluded from consideration.

Conflict of interest statement

G.P. is an employee of Polgenix, Inc. K.P. is CSO at Polgenix Inc. and an inventor of U.S. Patent No. 7706863 – "Methods for assessing a physiological state of a mammalian retina", and U.S. Patent No. 8346345 B2 – "Methods for assessing a physiological state of a mammalian retina" with values that may be affected by this publication.

Author contributions

N.S.A, G.P., and K.P. conceived the project. G.P. carried out imaging experiments. N.S.A developed the software. N.S.A, G.P., and K.P. wrote the manuscript.

Acknowledgments

We thank Dr. Leslie T. Webster, Jr for insightful comments on this manuscript. This work was supported by funding from the National Institutes of Health EY025451 and EY024864 (KP), the Arnold and Mabel Beckman Foundation, and Ohio Third Frontier (State of Ohio) TECG20150049. N.S.A is supported by the National Eye Institute of the NIH through grant 1K99EY025007. K.P. is John H. Hord Professor of Pharmacology.